Single-neutron removal reactions from ^{15}C and ^{11}Be: Deviations from the eikonal approximation

J. A. Tostevin,[1] D. Bazin,[2] B. A. Brown,[2,3] T. Glasmacher,[2,3] P. G. Hansen,[2,3] V. Maddalena,[2,3] A. Navin,[2,*] and B. M. Sherrill[2,3]

[1]*Department of Physics, School of Physics and Chemistry, University of Surrey, Guildford, Surrey GU2 7XH, United Kingdom*

[2]*National Superconducting Cyclotron Laboratory, Michigan State University, East Lansing, Michigan 48824*

[3]*Department of Physics and Astronomy, Michigan State University, East Lansing, Michigan 48824*

(Received 24 April 2002; published 23 August 2002)

The momentum distributions of the residual nuclei after one-neutron removal have been measured in coincidence with gamma rays identifying the distributions associated with the excited and ground state levels of these residues. These differential partial cross sections map the momentum content of the removed-nucleon wave functions and their description provides an exacting test of the reaction dynamics. Momentum distribution data when populating the ^{14}C and ^{10}Be ground states show a low-high momentum asymmetry that is incompatible with the hitherto used eikonal descriptions. A fully dynamical coupled discretized continuum channels description of the elastic breakup mechanism is shown to provide an understanding of this new observation which is most pronounced for weakly bound, *s*-wave, nuclear halo states. This interpretation is clarified further by an analysis of the momentum distributions as a function of the angle of detection of the heavy ground state residues.

DOI: 10.1103/PhysRevC.66.024607 PACS number(s): 24.10.Eq, 25.60.Gc, 25.70.De, 27.20.+n

I. INTRODUCTION

Cross sections for one-nucleon removal reactions from secondary beams of short-lived exotic nuclei, by a light target nucleus, are measured to be large. With the advent of measurements in which these heavy fragments, following nucleon removal, are detected in coincidence with de-excitation photons it has become clear that a large fraction of observed cross sections results from transitions in which the projectile residue is left in an excited state. Such measurements of the ground and excited state partial cross sections have been shown to provide an efficient and effective tool for studies of the evolution of the dominant single-particle states in rare nuclei [1–6] at beam energies of the order of 50 MeV/nucleon or greater. The advantages of reactions using a light absorptive target, such as ^{9}Be, are twofold. First it ensures the reaction is dominated by the nuclear interaction and avoids ambiguities due to the long-standing theoretical problem of the simultaneous treatment of both nuclear and Coulomb reaction mechanisms. Second, the use of a low Z nuclear target introduces spatial localization of the reaction at the nuclear surface. Use of ^{9}Be in particular, with no bound excited states, essentially presents a black absorptive disk to the incident core of nucleons. The requirement of core survival, at near to beam velocity, then dictates that those contributing core-target paths are highly peripheral with the result that the removed nucleon's wave function is probed at and beyond the surface of the projectile. This is then a very similar situation to that in low-energy light-ion transfer reactions on medium mass nuclei where the short mean-free paths of the ions lead to strong surface localization.

The measured partial cross sections to individual final states and their distribution as a function of final momentum component in the beam direction, $d\sigma/dp_{\parallel}$, identify both the orbital angular momenta of the removed nucleons and their spectroscopic factors. A review of the analyses to date, at beam energies less than 100 MeV/nucleon, can be found in Ref. [7] and the most recent analysis, of silicon and sulphur isotopes, in Ref. [8]. A very recent application [9] of this technique to data at higher energies, between 250 MeV/nucleon and 2 GeV/nucleon, where the reaction theory input is on a yet stronger footing, derives spectroscopic factors for proton removal in excellent agreement with those of the $(e,e'p)$ reaction [10], while extending the spectroscopic possibilities also to neutron removal and to unstable species. A recent systematic study of a large number of psd-shell nuclei, where the core states were not identified, adds further support to the value of the technique [11]. However, the method is most powerful when the different core state contributions are resolved.

The ground state of ^{11}Be has a well-developed neutron halo with a neutron separation energy S_n of only 0.503 MeV and a wave function dominated by a $1s_{1/2}$ neutron single-particle component. A recent experiment by Aumann *et al.* [1] studied the ^{9}Be(^{11}Be, ^{10}Be$+\gamma$)X one-neutron removal reaction at 60 MeV/nucleon. A subtraction procedure was used to construct the cross section for those events without a ^{10}Be decay photon in coincidence, corresponding to the ^{10}Be(g.s.). Significantly, the resulting parallel-momentum distribution of the ground state to ground state partial cross section, $d\sigma/dp_{\parallel}$, showed a marked low-high momentum asymmetry with a low momentum tail to the measured distribution. Such a feature is incompatible with the straight-line, constant velocity assumptions made in the eikonal theory used in Ref. [1] and elsewhere for the analysis of such systems and which lead to symmetric distributions about the

*Permanent address: Nuclear Physics Division, BARC, Trombay, Mumbai 400 085, India.

momentum corresponding to the beam velocity. This suggests that the analysis and our understanding of these data and the underlying reaction mechanism is still incomplete. We should stress that the asymmetry under discussion here is that seen in the *exclusive* momentum distributions to the ground states of the residues. Low momentum tails can also be observed in inclusive momentum distributions [11], but there they almost certainly originate, not from intrinsic core state asymmetries, but from the overlapping core final state distributions with different $p_\parallel$ centroids. In the exclusive measurements to date [7] only the two ground state transitions discussed here have revealed significant asymmetry in the $p_\parallel$ distribution.

In this paper we show that an understanding of the observed ground state to ground state momentum distribution asymmetry is provided by using a fully dynamical description of the elastic breakup component of the cross section. A preliminary analysis of this effect was reported in Ref. [12]. The observations for ^{11}Be are also confirmed in a precise new experiment on ^{15}C, with $S_n = 1.218$ MeV. The low lying states of ^{15}C and their spectroscopy are rather well determined empirically. Two analyses of the ^{14}C(d,p) ^{15}C reaction, at 16 and 17 MeV, derive spectroscopic factors of 0.99 and 1.03 for the $1/2^+$ ground state neutron orbital [13,14]. A third 14-MeV experiment and analysis of Goss *et al.* [15] derives $S = 0.88$, but using a more extended neutron bound state potential geometry, with Woods-Saxon parameters $r_0 = 1.3$ fm, $a_0 = 0.7$ fm, which will enhance the calculated cross section and so reduce the extracted spectroscopic factor. The ^{15}C case is therefore a very useful test case with a relatively pure single-particle ground state.

A second new feature of this paper is an investigation of the dependence of the $d\sigma/dp_\parallel$ cross section distributions on the angle of the emerging core particle. We show here that this additional differential cross section, and the quantum mechanical elastic breakup calculations, suggest different angular distributions from the contributing stripping and elastic breakup reaction mechanisms. Consequently, although the observed asymmetry is expected to be most important for weakly bound and halo states, the results discussed have significance beyond halo states in the clarification of the two mechanisms contributing to single-nucleon removal reactions.

II. EXPERIMENTAL TECHNIQUES

Measurements of the one-neutron-removal reactions from ^{15}C were performed at the National Superconducting Cyclotron Laboratory (NSCL) at Michigan State University. A radioactive beam of ^{15}C was produced by fragmentation of an incident 80-MeV/nucleon ^{18}O primary beam on a thick ^{9}Be target. The secondary beam was purified in the A1200 fragment separator [16] by the combination of magnetic analysis and an intermediate degrader. The resulting beam was delivered to the experimental setup, shown in Ref. [6], consisting of three parts: a dispersion-matching beam line, a target surrounded by an array of NaI(Tl) gamma detectors [17], and the S800 spectrograph [18] used for detecting the projectile residues from the reaction.

A. Cross section and momentum distribution of the knockout residue

The A1200 separator has been designed to accept a large momentum bite, up to 3% in normal operation. Alternatively it is possible to perform high resolution experiments with such a beam through the use of a dispersion-matched system. In this the spread in incident momentum is compensated by dispersing the secondary beam on the reaction target and using the magnification of the spectrograph to cancel its dispersion. The S800 spectrograph [18] has been designed to operate in this way. Due to the large dispersion of the S800, the beam must be limited to a spread in relative momentum of 0.5%. In this case, it is possible to study reaction products at a relative momentum resolution of 0.025%. The spectrograph is characterized by a large angular acceptance (up to 20 msr solid angle, $\pm 5°$ horizontal, $\pm 3.5°$ vertical, dispersive direction) and by a momentum acceptance of $\pm 2.5\%$. The position and angles of the fragments were determined by two x/y position-sensitive cathode-readout drift chambers [19] at the focal plane of the spectrograph. The resulting beam of ^{15}C was cleanly identified on an event-by-event basis with a typical intensity of 90 particles per second. The reactions took place in a secondary target of 228 mg/cm^2 ^{9}Be at a mid-plane energy of 54 MeV/nucleon. The resolution and intensity of the incident secondary beam was monitored in short exposures with the setting of the spectrograph adjusted to the full momentum of the ^{15}C beam. After this, long exposures at an appropriately reduced field setting identified the ^{14}C residues. Their full momentum distributions were reconstructed with the ion optics code COSY INFINITY [20]. The intensities of the beams and residues were normalized using the signals from a beam-line timer, a scintillator placed at the end of the A1200 separator.

At the focal plane of the S800, a segmented ionization chamber and a 5-cm-thick plastic scintillator measured the energy, energy loss, and time of flight of the residues. These data were used for particle identification purposes. The cross section for the one-neutron removal reaction was calculated as the yield of detected fragments divided by the yield of incident projectiles, taking into account the thickness and number density of the ^{9}Be target. The spectrograph acceptance provided a complete momentum distribution for the narrow distributions corresponding to the $l_0 = 0$ state component, and the corrections for the angular and the momentum acceptance in the $l_0 = 1$ orbital angular momentum distribution were small. The procedure has been discussed in Ref. [6]. The absolute partial cross sections were obtained from the gamma-ray data as described below. The error of 12% in the total one-neutron removal cross section includes uncertainties in target thickness, incident particle rate, particle identification, and acceptance. In the following, the momentum distributions are shown in the laboratory system, and the measured quantity is actually the total momentum, which has been projected onto the beam axis to give the quantity $p_\parallel$ used in the figures of the present paper. Since the residue's deflection angle is small, typically a few degrees, the difference between the total momentum and the parallel momentum is small. The laboratory distributions are broadened by

the relativistic γ factor, which has to be included in the comparisons with theory.

B. Gamma-ray detection

The excited states of the residues were tagged by an inner ring of 11 cylindrical NaI(Tl) scintillators surrounding the target. Each scintillator was read out by two photomultiplier tubes, one at each end, thus allowing the determination of both the energy and the interaction point of the photon in the detector. The position information provided by the array made it possible to correct for the Doppler shift in the energy of the γ rays emitted by the fast ($\beta \simeq 0.33$) residues. The energies of up to four hits in separate detectors were added independently to the spectrum, so that summing of coincident lines in this large detector was greatly reduced. The back transformation to the center of mass (c.m.) system, however, does not generate the spectrum that would have been observed from a source at rest due to the energy dependence of the detection efficiency and, especially, events in which radiation has escaped from the crystal. Examples of these are annihilation radiation and Compton-scattered photons. Since the reconstruction cannot identify these features, the part of the response function that lies below the full-energy peak gets distorted. This may seem unimportant since the full-energy peaks obviously are reconstructed correctly. However, an accurate understanding of the measured envelope of the gamma spectrum requires knowledge also of the shape of the continuum distributions underlying the peaks. For the decomposition of the measured spectrum, complete response functions were constructed in a numerical simulation in the following way.

For a gamma ray of a given energy, assumed to be isotropically emitted in the projectile c.m. system, a sequence of Lorentz-boosted γ events with the appropriate angular distribution was generated in a Monte Carlo procedure. These were subsequently used in the Monte Carlo code GEANT [21], which simulated the energy deposited in the detectors as well as losses generated by interactions with chamber walls and detector mounts. One million events were generated for a given energy. For each event the (random) outcome was randomly broadened by the energy resolution, which was assumed to scale with the square root of the energy and was fixed to the measured resolution corresponding to a full width at half maximum (FWHM) of 7.5% at 1.33 MeV. Based on the spatial resolution of 1.5 cm FWHM, the sequence of simulated γ signals were corrected event by event for the Doppler shift to construct the apparent energy in the c.m. system. Histograms of the simulated events created the reference line shapes, which were used for fitting the observed spectra. The reliability of the simulations was verified by comparing measured and simulated γ-ray spectra from (necessarily stationary) calibration sources. An agreement to within 10% in the absolute intensity was found.

A complication in the data analysis was the presence of a continuum background distribution varying approximately exponentially with energy. This has been discussed in Ref. [6], which shows results from the isotopes ^{11}Be and ^{16}C, which have no gamma rays above 0.8 MeV. This projectile-related background is attributed to neutrons, gamma rays, and charged particles produced in the target and to their secondary interactions with construction materials and the scintillators. Its intensity for gamma energies above 0.25 MeV is approximately 9% per outgoing fragment and the same for the two isotopes. It has been included with the same absolute intensity per incident fragment in the analysis of the ^{15}C gamma spectrum shown in Fig. 1. The measured branching ratios deduced from the gamma intensities (with indirect feeding taken into account) are given in Table I. Those for the previously reported ^{11}Be experiment can be found in Table I of Ref. [1].

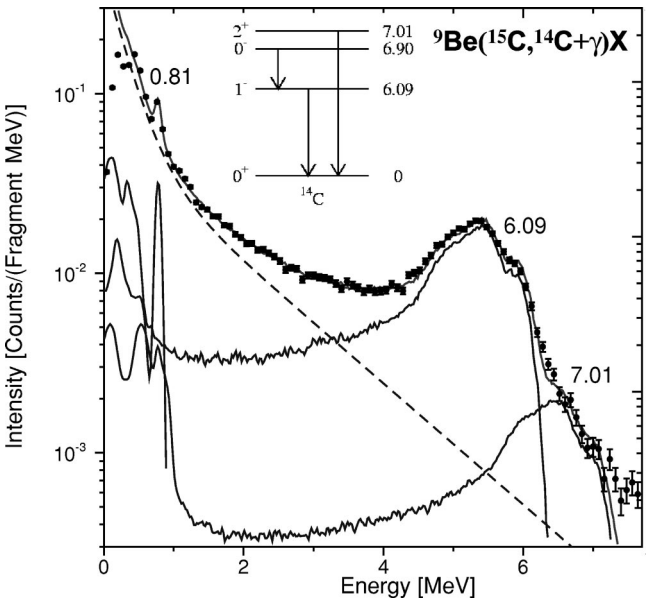

FIG. 1. Center-of-mass system γ-ray spectrum from ^{9}Be(^{15}C, ^{14}C+γ)X (filled circles) and its decomposition into individual line shapes obtained in the Monte Carlo simulation. The 0.81- and 6.09-MeV gamma rays are in cascade and give rise to a sum line at 6.90 MeV. There is no crossover. Since the spectrum was analyzed on the basis of individual hits in the detectors, this sum line is much weaker than the 7.01-MeV gamma ray, which we attribute to a known 2^+ level in ^{14}C. The approximately exponential component is the continuum contribution ascribed to neutrons and gamma rays from the target. Its intensity and shape has been taken from Ref. [6].

III. REACTION THEORY MODELS

The data for the momentum distributions to the ground and 6.09-MeV 1^- states of ^{14}C are shown in Fig. 2. These are each the sum of cross sections from two distinct reaction mechanisms. The first, stripping, involves the removed nucleon being absorbed by the target and hence being removed from the forward-going beam—the inclusive cross section for target excitation. The second, diffraction dissociation or elastic breakup of the projectile, describes the separation of the neutron from the core by the neutron- and core-target tidal forces, the target remaining in its ground state. Both of these processes must therefore be calculated and cannot be individually identified from the measurements made only of the residue.

The single-particle stripping contribution to the cross sec-

TABLE I. Cross sections (in mb), theoretical and deduced spectroscopic factors for the reaction ^{9}Be(^{15}C, ^{14}C(I^π))X at $E=54$ MeV/nucleon. The ^{15}C ground state spin is $J^\pi=\frac{1}{2}^+$. The division of cross section between the stripping and diffraction dissociation mechanisms is also shown. The lower entries in the table show eikonal calculations (i) for the ground state transition when using the Woods-Saxon ^{15}C(g.s.) single-particle wave function and the JLM neutron-^{9}Be optical potential, and (ii) the ground state and 1^- transitions when the ^{15}C single-particle wave functions are calculated from the Skyrme HF (see text). The 1^- and 0^- final state results were calculated assuming a ^{13}C+$n(1s)$ composite core [3].

E[MeV]	I^π	l_0	σ_{sp}(str)	σ_{sp}(diff)	σ_{sp}	σ_{exp}	C^2S_{exp}	C^2S_{th}
0.00	0^+	0	91	56	147[a]	109 ± 13	0.74 ± 0.09	0.98
6.094	1^-	1	23	8	31[a]	22 ± 3	0.72 ± 0.10	1.18
6.903	0^-	1	22	7	29[a]	3 ± 1	0.10 ± 0.03	0.46
7.102	2^+	2	23	7	30[a]	3 ± 1	0.10 ± 0.03	0.02
					σ_{tot}	137 ± 16		
0.00	0^+	0	63	67	130[b]	109 ± 13	0.84 ± 0.10	0.98
0.00	0^+	0	76	45	121[c]	109 ± 13	0.90 ± 0.10	0.98
6.094	1^-	1	21	7	28[c]	22 ± 3	0.79 ± 0.11	1.18

[a]Cross sections from the Glauber model potential and WS single-particle wave functions.
[b]Cross sections from the JLM potential and WS single-particle wave functions.
[c]Cross sections from the Glauber model potential and HF single-particle wave functions.

tion, σ_{sp}(str), was discussed by Hussein and McVoy [22] and Hüfner and Nemes [23] in the spectator core model and an expression given within the eikonal limit. This still represents one of the only practical ways to calculate this inclusive cross section with respect to target excitations. The transfer to the continuum based approach of Bonaccorso and Brink [24] has much in common with the eikonal approximation for the stripping term. Although quantum mechanical few-body formalisms applicable to the stripping part of the cross section have been proposed (a review has been given by Ichimura [25]) these have not led to practical implementations. In the present work all calculations of the stripping terms will use the eikonal formalism [26,6].

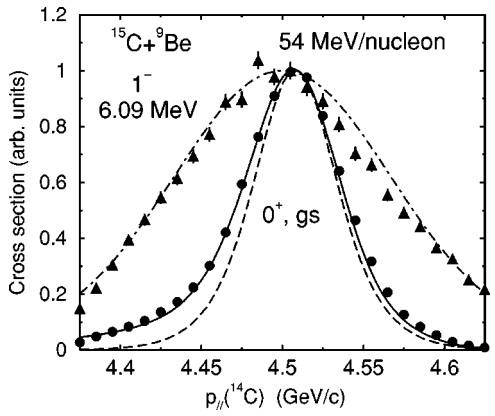

FIG. 2. Distributions with the parallel momentum $p_\parallel$ of the cross section to the ground state of ^{14}C (circles) and in coincidence with the 6.094-MeV gamma ray (triangles). (The latter contains a 10% contribution from feeding via the 6.90-MeV level. Coincidences with the 0.81-MeV gamma ray show this contribution, within the experimental errors, has the same $l_0=1$ shape.) Acceptance corrections are discussed in Ref. [6]. They amount to a factor 2 at the edges of the figure. The dashed (g.s.) and dot-dashed (1^-) curves are the results of the eikonal-model calculations with the peak heights and positions adjusted to the data. (The theoretical 1^- peak has been centered 0.008 GeV/c lower than that of the ground state. The calibration was not precise enough to permit a discussion of the absolute position of the peaks relative to beam velocity.) The solid curve for the ground state transition is the result of the CDCC analysis discussed in the text.

Practical methods for calculations of the diffraction dissociation (or elastic breakup) component σ_{sp}(diff) of the neutron removal cross section are much better developed, since this is an exclusive process. These include the coupled discretised continuum channels (CDCC) [27] and eikonal methods (used here), time-dependent [28,29], distorted waves Born approximation (DWBA) [30] and numerous first- and higher-order semiclassical formulations [28,31]. We will show that for the nuclear breakup of the weakly bound projectiles discussed here the DWBA approximation is not sufficiently accurate and that reliable calculations of σ_{sp}(diff) require a higher-order treatment. Use of the CDCC approach includes such higher-order effects. Most importantly it guarantees a complete dynamical description of the energy transfer between the c.m. and internal degrees of freedom of the reacting projectile, expected to be vital for the study of finer details of the momentum distributions of the residues.

To date, at the fragmentation beam energies of interest here, $\approx$50 MeV/nucleon and greater, theoretical analyses have, almost exclusively, exploited the sudden/adiabatic plus eikonal approximations. These lead to considerable practical simplifications and to calculation schemes [3,6] with relatively simple and transparent physical inputs. They have been very successful [24,26,32,33], with good agreement between different models.

A. Eikonal model cross sections

The eikonal reaction theory of Refs. [3,6] has been used here to calculate the single-particle removal cross sections $\sigma_{sp}[=\sigma_{sp}(\text{str})+\sigma_{sp}(\text{diff})]$ shown in Table I. The removed

nucleon-core bound state wave functions are calculated in a Woods-Saxon potential well with conventional radius and diffuseness parameters 1.25 and 0.7 fm [6]. The depth of the potential is adjusted to reproduce the physical separation energy of the nucleon from the projectile for each residue final state. The neutron- and core-target interactions are calculated by single and double folding, respectively, of the effective Gaussian nucleon-nucleon interaction of [3] assuming Gaussian matter distributions for the core and target. We assume root mean squared mass radii of 2.30, 2.28, and 2.28 fm for ^{14,13}C and ^{10}Be. For the transitions to the excited final states of the ^{14}C core, in which a more tightly bound core neutron is removed, the ^{14}C core is itself treated as a composite, of ^{13}C and the weakly bound *s*-wave valence neutron, as was discussed in Ref. [3].

Based on the $B(E1)$ distributions calculated from the ground state single-particle wave functions, upper bounds on the Coulomb dissociation contribution to the ground state to ground state cross sections are estimated to be less than 10 mb for ^{11}Be and 4 mb for ^{15}C, compared to the measured cross sections of 203(31) mb and 109(13) mb, respectively. These small Coulomb contributions will not be considered further in this paper.

As has been noted earlier [12], the eikonal model σ_{sp} are relatively insensitive to the details of the assumed nucleon-target interaction, provided they give consistent nucleon-target reaction cross sections. However, the division of cross section between the diffractive and stripping mechanisms is sensitive to the choice of potential. A realistic description of the refractive (real) content of the neutron-target optical potential is therefore rather essential for a quantitative study of the relative contributions from the stripping and elastic breakup mechanisms. The optical limit profile function for the nucleon-target system constructed above is less obviously appropriate for comparisons with the CDCC calculations which also, for practical purposes, require specification of a neutron-target optical interaction. We therefore make use of the better theoretically founded microscopic effective nucleon-nucleus interaction of Jeukenne, Lejeunne, and Mahaux [34] (JLM), shown to provide a good overall description of a large body of nucleon scattering data from light and medium mass nuclei at these energies [35]. So, in the CDCC calculations, the neutron interaction with the target is calculated from the same target density, the mid-point local density approximation [35], and the JLM effective interaction. We apply the conventional scalings, 1.0 and 0.8, to the real and imaginary strengths [35] of the calculated interaction. To allow a more direct comparison with these calculations, the eikonal calculations were repeated with this neutron interaction, the neutron-target profile function being calculated using the exact continued phases method of Ref. [36]. These eikonal calculations are also shown in Table I for the ground state transition only. The more refractive and less absorptive nature of the JLM optical potential is reflected in the reduced stripping and enhanced diffractive cross section contributions with the JLM interaction, shown in Table I.

We note that, being consistent with earlier analyses [1–6], we have used a fixed Woods-Saxon potential geometry, with radius 1.25 fm and diffuseness 0.70 fm, to generate the single-particle bound states. This common choice has allowed a systematic study of the many measured transitions without parameter variation in individual cases, and has led to a consistent overall agreement of theoretical shell model and experimentally deduced spectroscopic factors [7]. It is also clear, however, that the absolute nucleon removal cross sections will be sensitive to these bound state wave functions. To gain an insight into this sensitivity in the ^{15}C case, we have also recalculated the reaction using single-particle wave functions from a Skyrme Hartree-Fock (HF) calculation [37]. It was necessary to scale the central HF potential, by a number near unity, to ensure agreement with the empirical separation energy for each orbital [38]. In the surface and tail regions, of importance to nucleon removal reactions, this wave function is very similar to that calculated in a modified Woods-Saxon geometry of radius 1.27 fm and diffuseness 0.50. The smaller diffuseness reduces the rms radius of the 1*s* orbital and hence the calculated neutron removal cross section, to 121 mb. The 1^- state cross section is less affected, being reduced by only 2.5 mb.

The different eikonal model cross sections are collected in Table I and give an overview of the model sensitivities in the calculated σ_{sp}. The resulting experimental spectroscopic factors to the lowest two states are in reasonable agreement with the theoretical shell model values from the WBP interaction [39]. The radial mismatch factors, which account for the change in average potential for the neutron in the projectile and residual nuclei [4], are within 2% of unity for the 1^-, 0^-, and 2^+ states and so have no implications in this case. We will return to a discussion of the ground state spectroscopic factor in Sec. V. The experimental cross section to the 6.903-MeV 0^- state falls short of that expected theoretically, but a discussion of the spectroscopy of these higher lying states is not the priority of this work and will not be entered into here.

B. Parallel momentum distributions

The shapes of the measured $d\sigma/dp_{\|}$ distributions for nucleon removal from ^{15}C leaving ^{14}C in its ground or 6.09-MeV 1^- levels are shown in Fig. 2. As was discussed in the introduction, a characteristic of these reactions is their surface dominance, evident from the facts that (i) the calculated stripping cross sections shown in Table I are much smaller than the free neutron-target reaction cross section, $\approx$300 mb, and (ii) the momentum components associated with the inner lobe of the 1*s* neutron wave function are absent from the ground state momentum distributions in Fig. 2 [40].

Eikonal estimates of the $d\sigma/dp_{\|}$ are also shown by the dashed and dot-dashed curves, based here on profile functions with sharp cutoff radii, chosen to reproduce the free neutron-target and core-target reaction cross sections. The calculations assume, as is usual [41], that the stripping and diffractive cross section components have the same shape. The experimental distribution to the 6.09-MeV 1^- level agrees well with the eikonal calculation (dot-dashed curve). While the eikonal calculation (dashed line) clearly identifies the ^{14}C(g.s.) distribution as due to *s*-state nucleon removal

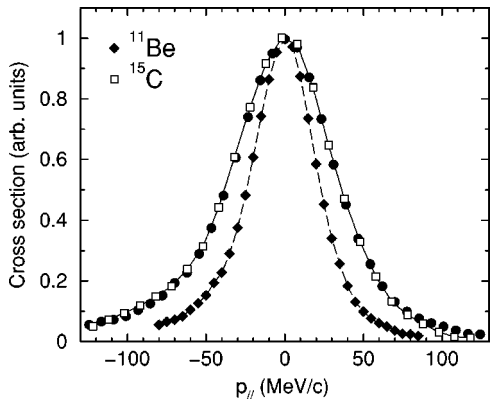

FIG. 3. Comparison of the measured parallel momentum distributions, in the projectile rest frame, for populating the ^{14}C(g.s.) (open squares) and ^{10}Be(g.s.) (filled diamonds) in nucleon removal from ^{15}C and ^{11}Be at 54 and 60 MeV, respectively. The lines are a guide to the eye. The filled circles show the result of scaling the width of the ^{10}Be distribution by the square root of the ratio of the separation energies in the two cases, $\sqrt{(1.218/0.503)}$.

its failure in detail is quite apparent. The ground state data show an increased width and an excess of intensity at low momenta when compared to the eikonal theory (dashed curve), as was seen also for the ^{11}Be data [1], shown by the filled diamonds in Fig. 3. The width of the calculated eikonal distribution has been shown to retain a very small sensitivity to the details of the profile functions used [42] but cannot lead to asymmetry.

Our concern is this observed asymmetry. These first indications of a systematic departure from the eikonal theory are evident only because of the exclusive character and quality of the data shown in Fig. 2 and Ref. [1]. In Fig. 3 we also show that these observed asymmetries in ^{15}C (open squares) and ^{11}Be (filled diamonds) must have a common origin since their ground state distributions, and their associated asymmetries, are essentially identical when the widths of the distributions are scaled by their ground state bound-neutron asymptotic wave number. The filled circles, obtained when the width of the ^{11}Be distribution is rescaled by $\sqrt{1.218/0.503}$, are essentially identical with those for the ^{15}C. This scaling is what the simplest sudden approximation model would predict if the bound *s* states were approximated by Yukawa wave functions.

A feature of the semiclassical eikonal approximations is that they are implicitly energy nonconserving. The calculations do not treat energy sharing between the center of mass and relative motion degrees of freedom of the neutron and core or the momentum transfers involved in the deflection of the core from its assumed (eikonal) straight line path. A result is that the calculated distributions must be symmetric about the momentum corresponding to the beam velocity. That the experimental asymmetry is pronounced for the halo states suggests that the phenomenon is associated with the elastic breakup mechanism and that there is a need to go beyond the eikonal theory.

IV. COUPLED CHANNELS BREAKUP CALCULATIONS

In the present work, we exploit the fully quantum mechanical coupled discretized continuum channels (CDCC) method [27] to calculate the elastic breakup components of the ^{15}C and ^{11}Be nucleon removal cross sections. The CDCC approach calculates a three-body solution of the Schrödinger equation, an approximate description of the projection of the full many-body wave function onto the ground states of the target and core nuclei. The target *t* is assumed here to have spin zero and no explicit target excitation is included, so effects of target excitation on the elastic breakup enter only through the complex effective interactions of the core and valence neutron with the target. Here $\vec{R}$ is the position of the c.m. of the core and neutron relative to the target and $\vec{r}$ is the position of the removed-neutron relative to the core.

The core particles *c* in the present case are spinless, and the neutron has spin *s* and projection σ. These particles are assumed structureless. The total angular momentum of the projectile ground state is *I*, with projection *M*, in which the relative orbital angular momentum of the two constituents is l_0 and their separation energy is $\mathcal{E}_0(>0)$. The incident wave number of the projectile in the c.m. frame of the projectile and target is $\vec{K}_0$ and the coordinate *z* axis is chosen in the incident beam direction.

In the CDCC treatment of the breakup of neutron-core systems one couples the incident projectile in spin state (I,M), in all orders, to selected breakup configurations (I',M') of the core and neutron, with relative orbital angular momentum *l*. This continuum of breakup states, in each significant spin-parity excitation I', is further grouped into a number $\mathcal{N}(I')$ of representative energy intervals or bins. In each bin *i*, representing states with wave numbers on the interval $[k_{i-1}\rightarrow k_i]$, a square integrable bin state $\hat{\phi}_\alpha, \alpha \equiv (i,(ls)I')$ is constructed [43] as a weighted superposition of the scattering states in that interval. In the present applications, orbital angular momenta $l\leqslant 5$ are included and lead to converged results. In each I' channel, $\mathcal{N}=10$ bins were used. This CDCC model space, for the ^{15}C case, is shown schematically in Fig. 4. The widths of the bins in each *l* channel, extending up to the maximum relative energies indicated, are chosen so that each bin spans an equal relative wave number interval.

A. Construction of continuum bin states

For each of the $\mathcal{N}(I')$ bin intervals, with width $\Delta k_i = [k_i - k_{i-1}]$, the representative bin state is, explicitly,

$$\hat{\phi}_\alpha^{M'}(\vec{r}) = [Y_l(\hat{r}) \otimes \mathcal{X}_s]_{I'M'} u_\alpha(r)/r. \tag{1}$$

Each radial function u_α is a square integrable superposition with weight function $g_\alpha(k)$,

$$u_\alpha(r) = \sqrt{\frac{2}{\pi N_\alpha}} \int_{k_{i-1}}^{k_i} g_\alpha(k) f_\alpha(k,r)\, dk, \tag{2}$$

of the scattering states $f_\alpha(k,r)$, eigenstates of the $c+n$ relative motion Hamiltonian H_p. The normalization factor is $N_\alpha = \int_{k_{i-1}}^{k_i} |g_\alpha(k)|^2 dk$. The f_α are defined here such that, for $r\rightarrow\infty$,

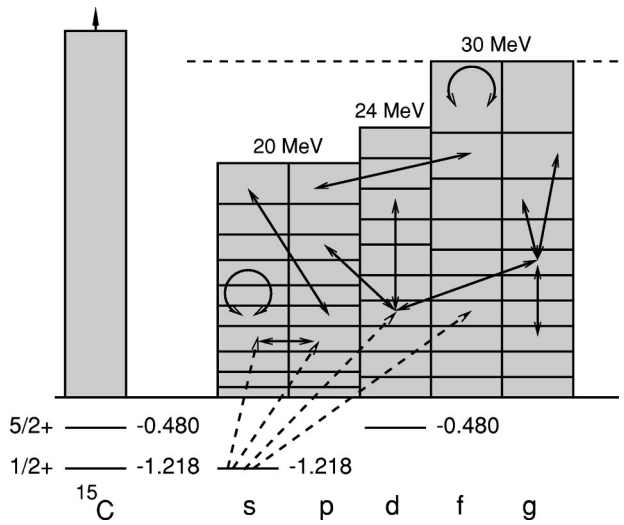

FIG. 4. Diagrammatic representation of the CDCC model space calculation for ^{15}C. The left side shows the physical bound states and continuum and the right hand side the included continuum bins (10) in each $n+^{14}$C partial wave. The dashed arrows are representative of the one-way couplings included in the DWBA. The solid arrows show representative couplings for the full CDCC calculations which connect all bins, including diagonal bin couplings, with two-way couplings to all orders. Relative *h* waves were found to make negligible contributions.

$$f_\alpha(k,r)\rightarrow[\cos\delta_\alpha(k)F_l(kr)+\sin\delta_\alpha(k)G_l(kr)], \quad (3)$$

where k belongs to bin α and F_l and G_l are the regular and irregular partial wave Coulomb functions. So the f_α are real when using a real $c+n$ two-body interaction. Energy conservation connects the wave numbers K_α of the c.m. of the fragments in bin state α and the corresponding bin state excitation energies $\hat{\mathcal{E}}_\alpha=\langle\hat{\phi}_\alpha|H_p|\hat{\phi}_\alpha\rangle$. For non-*s*-wave bins we used $g_\alpha(k)=1$. For the *s*-wave bins we used $g_\alpha(k)=k$ which aids the interpolation of the three-body transition amplitude near the breakup threshold.

These bin states $\hat{\phi}_\alpha$ provide an orthonormal relative motion basis for the coupled channels solution of the three-body $c+n+t$ wave function. The bins and their coupling potentials $\langle\hat{\phi}_\alpha|U(\vec{r},\vec{R})|\hat{\phi}_\beta\rangle$ are constructed, and the coupled equations are solved, using the coupled channels code FRESCO [44]. Here $U(\vec{r},\vec{R})$ is the sum of the interactions of the core and neutron with the target, which are expanded to multipole order q. The coupled equations solution generates (effective two-body) transition amplitudes $\hat{T}^{\alpha}_{M'M}(\vec{K}_\alpha)$, already summed over projectile-target partial waves, for populating each bin state I',M' from initial state I,M, as a function of the angle of the c.m. of the emerging excited projectile in the c.m. frame. These amplitudes are expressed in a coordinate system with x axis in the plane of $\vec{K}_0$ and $\vec{K}_\alpha$. For a general x-coordinate axis the coupled channels amplitudes must subsequently be multiplied by $\exp(i[M-M']\phi_K)$, with ϕ_K referred to the chosen x axis.

B. Three-body breakup observables

The relationship of the CDCC coupled channels bin state inelastic amplitudes $\hat{T}^{\alpha}_{M'M}(\vec{K}_\alpha)$ to the physical breakup transition amplitudes $T_{\sigma:M}(\vec{k},\vec{K})$ from initial state I,M to a three-body continuum final state is discussed in detail in Ref. [43]. This is needed to make predictions for the detection geometries considered here, since each detector configuration and detected fragment energy involves a distinct final state c.m. wave vector $\vec{K}$, breakup energy $\mathcal{E}_k$, and relative motion wave vector $\vec{k}$.

The three-body breakup T matrix can be written

$$T_{\sigma:M}(\vec{k},\vec{K})=\frac{(2\pi)^{3/2}}{k}\sum_{\alpha\nu}(-i)^l(l\nu s\sigma|I'M')\times\exp[i\delta_\alpha(k)]\times Y^\nu_l(\hat{k})g_\alpha(k)T_{M'M}(\alpha,\vec{K}). \quad (4)$$

Here $\delta_\alpha(k)$ is the neutron-core relative motion phase shift in excitation state I', and the $T_{M'M}(\alpha,\vec{K})$ are interpolated from the coupled channels $\hat{T}^{\alpha}_{M'M}(\vec{K}_\alpha)$ on the chosen K_α and θ_{K_α} grid. Specifically,

$$T_{M'M}(\alpha,\vec{K})=\exp(i[M-M']\phi_K)[\hat{T}^{\alpha}_{M'M}(\vec{K})/\sqrt{N_\alpha}], \quad (5)$$

where the value of the bracketed term on the right hand side is interpolated from the coupled channels solution. The number of bin states used to describe each I' excitation must allow an accurate interpolation of these amplitudes. The sum in Eq. (4) is taken over all bin states α which contain k.

The three-body amplitudes, Eq. (4), are used to compute the triple differential cross sections for breakup in the laboratory frame. If the energy or momentum of the core particle is measured then the relevant cross section is

$$\frac{d^3\sigma}{dE_c d\Omega_c d\Omega_n}=\frac{2\pi\mu_{pt}}{\hbar^2K_0}\frac{1}{(2I+1)}\times\sum_{\sigma M}|T_{\sigma:M}(\vec{k},\vec{K})|^2\rho(E_c,\Omega_c,\Omega_n), \quad (6)$$

where $\rho(E_c,\Omega_c,\Omega_n)$ is the three-body phase space factor [45]. The data under discussion here are the parallel momentum distributions for the heavy core fragments and the cross sections must be integrated numerically over all directions of the unobserved neutron. The core $d\sigma/dp_\parallel$ differential cross sections are computed by writing, after $d\Omega_n$ integration, in the laboratory frame

$$\frac{d\sigma}{d\vec{p_c}}=\frac{1}{m_c p_c}\frac{d^2\sigma}{dE_c d\Omega_c} \quad (7)$$

and then integrating over the required angular acceptance and/or perpendicular momentum components of the heavy residue.

C. CDCC model space

The details of the model space parameters used in the CDCC calculations are as follows. Partial waves up to $L_{max}=200$ and radii R up to $R_{coup}=50$ fm were used for the computation of the projectile-target relative motion wave functions. The continuum bins were calculated using radii $r \leqslant r_{bin}=50$ fm.

In the final calculations presented, see Fig. 4, all l states up to and including g waves ($l=4$) were included. Addition of $l=5$ relative motion bins changed the calculated integrated elastic breakup cross sections for both the ^{15}C and ^{11}Be cases by less than 1 mb. The bin state discretization was carried out up to maximum relative energy $\mathcal{E}_{max}=20$ MeV in s and p waves, 24 MeV in d waves, and 30 MeV in f and g waves. The number of bins in each l configuration was 10 with equally spaced k_i from $k=0$ to k_{max}. In the case of the DWBA cross sections quoted below the calculations used the same model space, however, the ground state was coupled to each bin state in first order only. Calculations used potential multipoles $q \leqslant 4$ in constructing the coupling potentials and coupled equations set.

The core-neutron potentials used to construct the ground and continuum states were the standard spin-independent Woods-Saxon potential wells with radius parameter 1.25 fm and diffuseness 0.7 fm discussed earlier in Sec. III. In the $l=l_0=0$ states the well depth was chosen to reproduce the ground state neutron separation energies of 1.218 and 0.503 MeV for ^{15}C and ^{11}Be, respectively. The same potential was then used in all l configurations, except that the potentials in the p waves in ^{11}Be, and in the d waves in ^{15}C, were adjusted to reproduce the single bound excited states at 0.32 MeV ($p_{1/2}$) and 0.74 MeV ($d_{5/2}$) in the two systems. These bound channels were included as an additional state in the coupled channels calculations, together with the ground state entrance channel and the 50 bin state configurations. The inclusion of these single excited bound states had negligible influence on the breakup distributions and cross sections. The CDCC calculations are carried out assuming a ground state spectroscopic factor of unity.

The interactions used for the core-target systems were those which calculate the optical limit profile functions used in the eikonal calculations of Sec. III. Similarly, the potential of the neutron with the ^{9}Be target is the JLM interaction as was used in the eikonal calculation, also in Sec. III.

V. RESULTS

Figure 5 shows the calculated elastic breakup component of $d\sigma/dp_{\|}$ from the CDCC, for $^{15}\mathrm{C}+{}^{9}\mathrm{Be}\rightarrow{}^{14}\mathrm{C}(\mathrm{g.s.})+X$ at 54 MeV/nucleon, as a function of the maximum angle of detection of the ^{14}C residue in the laboratory frame. The cross section is that measured in a forward angle cone. Apparent is that the calculated cross section distribution is asymmetric, the asymmetry developing with the angle of the detected residues until the full cross section is obtained at about 4°. The solid circles, which have been scaled to the 0.5° acceptance curve, show the results of the eikonal calculation, the dashed curve from Fig. 2, and coincide with the CDCC distribution for these extreme forward angles of the residues, as would be expected. The integrated elastic breakup cross section from the CDCC is 56 mb, which compares with the value 67 mb computed in the eikonal model, Table I, with the same interactions. The corresponding DWBA calculation, in which all bin-bin and higher-order couplings are removed, generates an elastic breakup cross section of 65 mb. The calculations for ^{11}Be are qualitatively very similar. For the ^{11}Be case the elastic breakup cross sections obtained are 115 mb (CDCC), 185 mb (DWBA), and 127 mb (eikonal). These cross section values are tabulated in Table II.

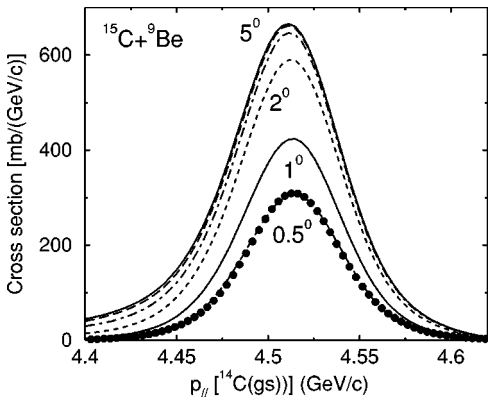

FIG. 5. Calculated elastic breakup component of $d\sigma/dp_{\|}$ for $^{15}\mathrm{C}+{}^{9}\mathrm{Be}\rightarrow{}^{14}\mathrm{C}(\mathrm{g.s.})+X$ at 54 MeV/nucleon from the CDCC as a function of the maximum angle of detection of the ^{14}C residue in the laboratory frame. The solid circles, scaled to the 0.5° acceptance curve, show the results of the eikonal calculation which coincide with the CDCC distribution for extreme forward angles of the residues.

To help clarify the relationship of the calculated and measured cross section asymmetry to the angle of acceptance of the detected core fragments, we calculate the core angle differential cross sections and momentum distributions $d\sigma/dp_{\|}d\Omega$. We consider the core fragments emerging in the laboratory angle intervals 0–1, 1–2, 2–3, and 3–4 degrees about the beam direction, both from the CDCC and from the experimental data. The ^{11}Be data of Ref. [1] have also been reanalysed in this differential form. Since the experiments did not use tracking of the incoming projectiles, the (rms) resolution on the deflection angle was only 0.43°. Our choice of one degree angular intervals here and in subsequent figures has been made to avoid contributions of this experimental resolution in the comparisons. The results for the differential cross sections are shown in Fig. 6. The corresponding experimental $d\sigma/dp_{\|}d\Omega$ for the ^{14}C(g.s.) and ^{10}Be(g.s.) transitions are shown by the solid symbols in Figs. 7 and 8. These show clearly that, as well as the expected fall of cross section with angle, there is both a broadening of the momentum distributions and a shift in the peak positions toward lower momenta with increasing scattering angle. We will return to calculations of these angle dependent distributions.

In Fig. 6 the experimental ground state partial cross sections in each angle interval are shown by the solid histograms, for both the ^{15}C (upper) and ^{11}Be (lower) induced reactions. These sum to the measured ground state nucleon removal cross sections of 109 and 203 mb, Table II. The

TABLE II. Calculated and measured neutron removal cross sections (in mb) and deduced spectroscopic factors for the reactions ^{9}Be(^{15}C, ^{14}C(0^+,g.s.))X at $E=54$ MeV/nucleon and ^{9}Be(^{11}Be, ^{10}Be(0^+,g.s.))X at $E=60$ MeV/nucleon. All calculations use the JLM neutron-^{9}Be optical potentials calculated from the target matter density discussed in Sec. III.

Projectile	Model	σ_{sp}(diff)	σ_{sp}(str)	σ_{sp}	σ_{exp}	C^2S_{exp}
^{15}C($1/2^+$)	CDCC	56	(63)[a]	119	109±13	0.92±0.11
	Eikonal	67	63	130		0.84±0.10
	DWBA	65				
^{11}Be($1/2^+$)	CDCC	115	(98)[a]	213	203±31	0.95±0.15
	Eikonal	127	98	225		0.90±0.14
	DWBA	185				

[a]Cross sections from the eikonal theory.

elastic breakup components to these differential cross sections predicted using the CDCC are shown by the dashed histograms and filled squares in the figure, summing to the values 56 and 115 mb, as stated above. This suggests that the cross section differences, 53 and 88 mb, are attributable to the stripping process in the two cases, to be compared with the eikonal calculation estimates of 63 and 98 mb. These revised calculated cross section values, and their implications for the experimentally deduced ^{15}C and ^{11}Be ground state spectroscopic factors, C^2S_{exp}, are collected in Table II. Within the 1σ experimental errors, C^2S_{exp} for ^{15}C is consistent with unity, and for ^{11}Be is consistent with the earlier analysis of Aumann *et al.* [1].

Evident from Fig. 6 is the generic nature of the ^{15}C and ^{11}Be results, the differences being essentially in the cross section magnitudes, driven by the neutron separation energies in the two cases. We note also that (i) the CDCC calculations predict that the measured cross sections for residues emerging at angles greater than 2° will be dominated by elastic breakup events, and (ii) that the stripping contributions, estimated as the difference between the experiment and the CDCC, are more forward angle focused. The figure also shows that, at the most forward angles, the stripping and elastic breakup contributions to the cross section are predicted to be approximately equal, a long standing expectation from eikonal model calculations at the energies involved here [26]. Although in principle calculable, at present we do not know the theoretically predicted stripping cross section contributions as a function of core angle. It would be interesting to compute this angular distribution for comparison with the expectations of Fig. 6.

The results in Fig. 6 also suggest that we should reasonably compare the largest angle $d\sigma/dp_{\|}d\Omega$ data of Figs. 7 and 8 directly with the CDCC calculations, assuming they arise from the diffraction dissociation mechanism alone. This is done in the lower (3–4°) solid lines in Figs. 7 and 8, revealing excellent agreement with the widths, magnitudes and the shifted peak positions of the experimental differential distributions. The conclusion here is that the CDCC calculation correctly predicts the breakup contributions into this

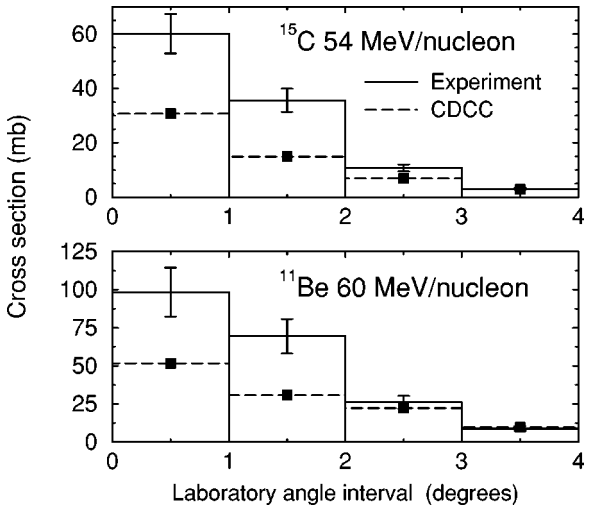

FIG. 6. Measured partial cross sections (solid lines) for population of the ^{14}C(g.s.) (upper) and ^{10}Be(g.s.) (lower) for residues emerging in the laboratory angle intervals indicated, from the ^{15}C + ^{9}Be and ^{11}Be + ^{9}Be reactions at 54 and 60 MeV/nucleon, respectively. The angle interval size of 1° has been chosen to avoid contributions of the experimental angular resolution in the comparison. The CDCC elastic breakup calculations are shown by the dashed lines and filled squares.

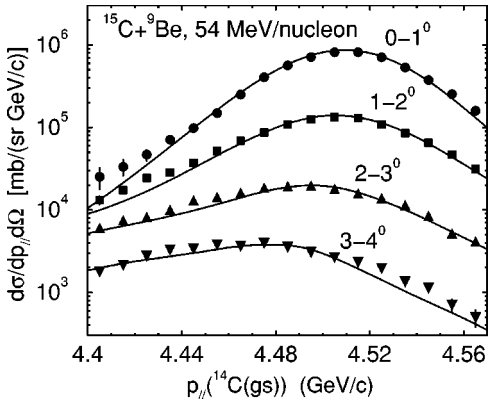

FIG. 7. Measured differential parallel momentum distributions (solid symbols) of the ^{14}C(g.s.) in each of the laboratory angle intervals indicated, from the ^{15}C + ^{9}Be reaction at 54 MeV/nucleon. The solid curves are the CDCC elastic breakup calculations supplemented, in the case of the 0–3° intervals, by the stripping cross section contributions required in Fig. 6. The latter have been added here assuming the same parallel momentum distribution for the stripping components as for the CDCC calculation.

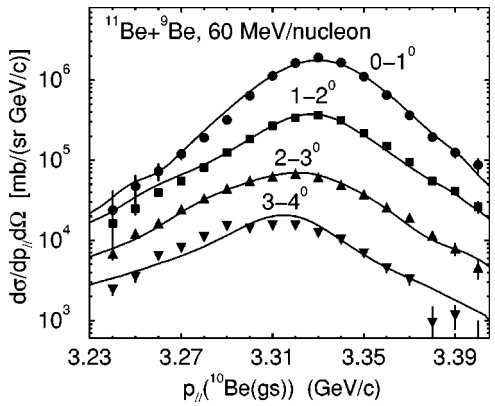

FIG. 8. Measured differential parallel momentum distributions (solid symbols) of the ^{11}Be(g.s.) in each of the laboratory angle intervals indicated, from the ^{11}Be+ ^{9}Be reaction at 60 MeV/nucleon. The solid curves are the CDCC elastic breakup calculations supplemented, in the case of the 0–3° intervals, by the stripping cross section contributions required in Fig. 6. The latter have been added here assuming the same parallel momentum distribution for the stripping component as for the CDCC calculation.

angle interval. Its correct treatment of energy and momentum conservation in the three-body dynamics also reproduce naturally the observed shift and width of the large angle $d\sigma/dp_{\parallel}d\Omega$ distributions, responsible in large part for the asymmetry in the data.

For the three smaller angle intervals the situation is a little more complex since we need to add an appropriate cross section contribution due to the stripping mechanism. Like the stripping cross section angular distribution itself, the shapes of the stripping components to the $d\sigma/dp_{\parallel}d\Omega$ distributions as a function of core angle are not known. Two available options are to assume (a) the same distribution as generated by the CDCC calculation, or (b) to apply the distribution calculated from the eikonal model at all core angles. In Figs. 7 and 8 the curves on the intervals from 0–3° are obtained when those stripping contributions indicated in Fig. 6 are added assuming these have the same shape as from the

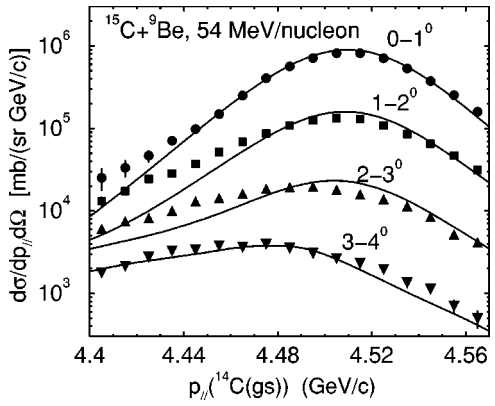

FIG. 9. As for Fig. 7 except that the stripping contributions to the 0–3° angle interval curves have now been assumed to have the parallel momentum distribution given by the eikonal calculation, shown in Fig. 2, and which is assumed independent of the angle of the residue.

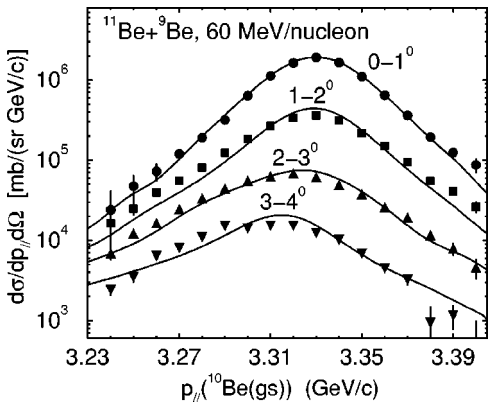

FIG. 10. As for Fig. 8 except that the stripping contributions to the 0–3° angle interval curves have now been assumed to have the parallel momentum distribution given by the eikonal calculation and which is assumed independent of the angle of the residue.

CDCC calculation which, among other processes, takes into account energy and momentum conservation in the deflection of the core fragment. The agreement with the data is excellent overall for both ^{15}C and ^{11}Be induced reactions. The solid curve for the angle inclusive ground state $p_{\parallel}$ distribution in Fig. 2 is the appropriate sum of these calculations, providing an excellent description of the measured asymmetry and width of the distribution.

If one uses instead the eikonal stripping $p_{\parallel}$ distribution shapes, shown in Fig. 2 for ^{15}C and in Ref. [1] for ^{11}Be, we obtain the revised theoretical distributions shown in Figs. 9 and 10. There is little to choose between the final $p_{\parallel}$ distributions with the two choices, however, using the elastic breakup (CDCC) distribution does lead, for both ^{15}C and

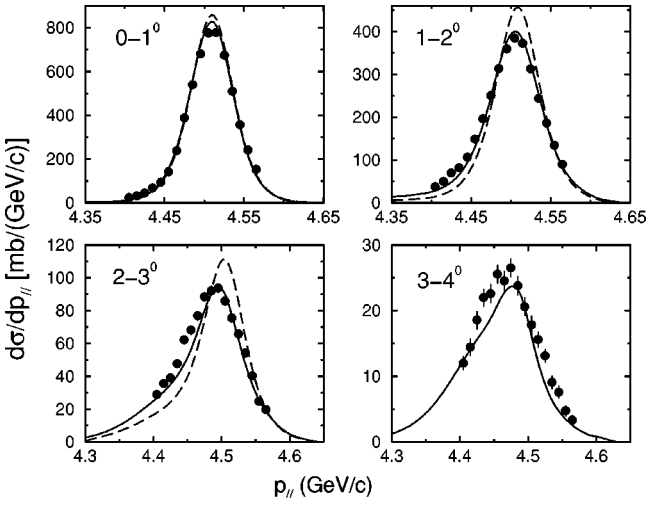

FIG. 11. The nucleon-removal parallel momentum distributions $d\sigma/dp_{\parallel}$, for the ^{15}C+ ^{9}Be reaction at 54 MeV/nucleon to the ^{14}C ground state, shown on a more familiar linear scale. The solid curves assume the stripping contributions have the same form as that calculated using the CDCC. The dashed curves assume the stripping contributions have a parallel momentum distribution at all angles of the residue given by the eikonal calculation shown in Fig. 2.

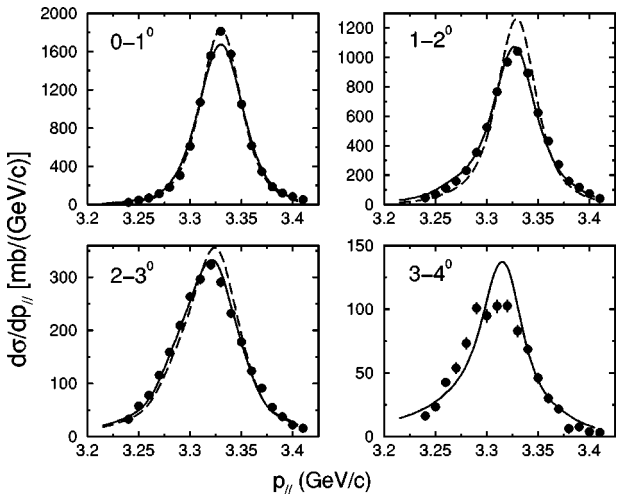

FIG. 12. The nucleon-removal parallel momentum distributions $d\sigma/dp_{\|}$, for the ^{11}Be+ ^{9}Be reaction at 60 MeV/nucleon to the ^{10}Be ground state, shown on a more familiar linear scale. The solid curves assume the stripping contributions have the same form as that calculated using the CDCC. The dashed curves assume the stripping contributions have a parallel momentum distribution at all angles of the residue given by the eikonal calculation.

^{11}Be, to an improved description of the data in the mid-angle region of 1–3°, particularly in the peak positions. This is shown in Fig. 11 for ^{15}C and Fig. 12 for ^{11}Be, where the angle-dependent $d\sigma/dp_{\|}$ are presented on a linear scale and where the stripping contributions have been added assuming CDCC (solid curves) or eikonal (dashed curves) shapes. The small but significant differences in the momentum distributions highlight the level at which the reaction mechanism is now being probed when the data are exclusive and of sufficient quality to make differential cuts. To carry the analysis further will require a more dynamically complete description of the target excitation (stripping) process to supplement that provided by the CDCC for the elastic breakup (diffractive) mechanism.

VI. CONCLUSIONS

In this paper we have examined in detail the integrated and differential cross sections, with respect to both parallel momentum and angle of the emerging heavy fragments, of neutron-removal reactions from the single neutron halo nuclei ^{15}C and ^{11}Be. A new experiment for the ^{15}C case is also reported. The momentum distributions of the ^{14}C and ^{10}Be ground state residues show a low-high momentum asymmetry that is incompatible with earlier eikonal model descriptions. CDCC calculations of the elastic breakup component of the reaction mechanism have been performed in both cases. We show how the CDCC approach is able to calculate the more general differential observables required to interpret the data.

Our partial cross section results, summarized in Tables I and II, show that the calculated absolute neutron removal cross sections and the deduced experimental spectroscopic factors show rather modest dependence on the details of the theoretical model. Moreover, the use of improved theoretical inputs, such as the CDCC elastic breakup treatment, the JLM neutron-target effective interaction, and of Skyrme Hartree-Fock neutron single-particle form factors for ^{15}C, each move the calculations toward a better agreement with the predictions of structure theory and the measurements in this important test case.

We show that the asymmetries observed in the ^{15}C and ^{11}Be parallel momentum distributions arise in a natural way from the CDCC theory with its exact treatment of the three-body breakup reaction dynamics. A detailed description of the available data is obtained, however, our lack of a fully dynamical description of the inclusive target excitation (stripping) component of the cross section leads to assumptions having to be made regarding the shape of the parallel momentum distribution, with angle, for this process. There are indications from the data that this distribution must have a similar shape to that from the CDCC.

Arising as they do from the elastic breakup mechanism, the physical effects discussed here are most pronounced for halo states. It will be important, however, to take these deviations from eikonal theory into account in transitions that require an accurate adjustment to mixed $l_0=0$ and 2 momentum profiles, such as have been observed in Refs. [5, 6]. Furthermore, the present analysis establishes that the reaction mechanisms in nucleon removal reactions can be understood in considerable detail and accurately described. This is an essential step in their use for mapping single-particle strength and the evaluation of structure theories in hitherto inaccessible regions of the nuclear chart.

ACKNOWLEDGMENTS

This work was supported by the Engineering and Physical Sciences Research Council, UK, Grant No. GR/M82141 and by the National Science Foundation under Grant Nos. PHY 0110253 and PHY 0070911.

[1] T. Aumann *et al.*, Phys. Rev. Lett. **84**, 35 (2000).
[2] A. Navin *et al.*, Phys. Rev. Lett. **81**, 5089 (1998).
[3] J.A. Tostevin, J. Phys. G **25**, 735 (1999).
[4] A. Navin *et al.*, Phys. Rev. Lett. **85**, 266 (2000).
[5] V. Guimarães *et al.*, Phys. Rev. C **61**, 064609 (2000).
[6] V. Maddalena *et al.*, Phys. Rev. C **63**, 024613 (2001).
[7] P.G. Hansen and B.M. Sherrill, Nucl. Phys. **A693**, 133 (2001).
[8] J. Enders *et al.*, Phys. Rev. C **65**, 034318 (2002).
[9] B.A. Brown, P.G. Hansen, B.M. Sherrill, and J.A. Tostevin, Phys. Rev. C **65**, 061601(R) (2002).
[10] G.J. Kramer, H.P. Blok, and L. Lapikas, Nucl. Phys. **A679**, 267 (2001).
[11] E. Sauvan *et al.*, Phys. Lett. B **491**, 1 (2000).
[12] J.A. Tostevin, Nucl. Phys. **A682**, 320c (2001).
[13] F.E. Cecil, J.R. Shepard, R.E. Anderson, R.J. Peterson, and P. Kaczkowski, Nucl. Phys. **A255**, 243 (1975).

[14] G. Murillo, S. Sen, and S.E. Darden, Nucl. Phys. **A579**, 125 (1994).
[15] J.D. Goss, P.L. Jolivette, C.P. Browne, S.E. Darden, H.R. Weller, and R.A. Blue, Phys. Rev. C **12**, 1730 (1975).
[16] B.M. Sherrill, D.J. Morrissey, J.A. Nolen, Jr., N. Orr, and J.A. Winger, Nucl. Instrum. Methods Phys. Res. B **70**, 298 (1992).
[17] H. Scheit, T. Glasmacher, R.W. Ibbotson, and P.G. Thirolf, Nucl. Instrum. Methods Phys. Res. A **422**, 124 (1999).
[18] B.M. Sherrill *et al.* (unpublished); J. A. Caggiano, Ph.D. thesis, Michigan State University, 1999.
[19] J. Yurkon, D. Bazin, W. Benenson, D.J. Morrissey, B.M. Sherrill, D. Swan, and R. Swanson, Nucl. Instrum. Methods Phys. Res. A **422**, 291 (1999).
[20] M. Berz, K. Joh, J.A. Nolen, B.M. Sherrill, and A.F. Zeller, Phys. Rev. C **47**, 537 (1993).
[21] GEANT, Cern Library Long Writeup W5013, 1994.
[22] M. Hussein and K. McVoy, Nucl. Phys. **A445**, 124 (1985).
[23] J. Hüfner and M.C. Nemes, Phys. Rev. C **23**, 2538 (1981).
[24] A. Bonaccorso and D.M. Brink, Phys. Rev. C **58**, 2864 (1998), and references therein.
[25] M. Ichimura, in *International Conference on Nuclear Reaction Mechanism, Calcutta, 1989*, edited by S. Mukherjee (World Scientific, Singapore, 1989), p. 374.
[26] K. Hencken, G.F. Bertsch, and H. Esbensen, Phys. Rev. C **54**, 3043 (1996).
[27] M. Kamimura *et al.*, Suppl. Prog. Theor. Phys. **89**, 1 (1986); N. Austern *et al.*, Phys. Rep. **154**, 125 (1987).
[28] H. Esbensen, in *International School of Heavy-Ion Physics, 4th Course: Exotic Nuclei*, edited by R.A. Broglia and P.G. Hansen (World Scientific, Singapore, 1998), p. 71.
[29] V.S. Melezhik and D. Baye, Phys. Rev. C **59**, 3232 (1999), and references therein.
[30] J.S. Al-Khalili and J.A. Tostevin, in *Scattering: Scattering and Inverse Scattering in Pure and Applied Science*, edited by E.R. Pike and Pierre C. Sabatier, (Academic, London, 2001), Chap. 3.1.3.
[31] G. Baur and H. Rebel, J. Phys. G **20**, 1 (1994).
[32] K. Yabana, Y. Ogawa, and Y. Suzuki, Phys. Rev. C **45**, 2909 (1992); Nucl. Phys. **A539**, 295 (1992).
[33] J.S. Al-Khalili, I.J. Thompson, and J.A. Tostevin, Nucl. Phys. **A581**, 331 (1995).
[34] J.-P. Jeukenne, A. Lejeunne, and C. Mahaux, Phys. Rev. C **16**, 80 (1977).
[35] J.S. Petler, M.S. Islam, R.W. Finlay, and F.S. Dietrich, Phys. Rev. C **32**, 673 (1985).
[36] J.M. Brooke, J.S. Al-Khalili, and J.A. Tostevin, Phys. Rev. C **59**, 1560 (1999).
[37] B.A. Brown, Phys. Rev. C **58**, 220 (1998).
[38] B.A. Brown, S. Typel, and W.A. Richter, Phys. Rev. C **65**, 014612 (2002).
[39] E.K. Warburton and B.A. Brown, Phys. Rev. C **46**, 923 (1992).
[40] P.G. Hansen, Phys. Rev. Lett. **77**, 1016 (1996).
[41] F. Barranco and E. Vigezzi, *International School of Heavy-Ion Physics, 4th Course: Exotic Nuclei*, (Ref. [28]), p. 217.
[42] Yu.L. Parfenova, M.V. Zhukov, and J.S. Vaagen, Phys. Rev. C **62**, 044602 (2000).
[43] J.A. Tostevin, F.M. Nunes, and I.J. Thompson, Phys. Rev. C **63**, 024617 (2001).
[44] I.J. Thompson, Comp. Phys. Rep. **7**, 167 (1988); FRESCO users' manual, University of Surrey, UK (unpublished).
[45] H. Fuchs, Nucl. Instrum. Methods Phys. Res. **200**, 361 (1982).